Institute of Nuclear and Particle Physics

EXPERIMENTAL REPORT ON PARTICLE IDENTIFICATION WITH THE $\Delta E - E$ SETUP

Gaurav Singh: gsingh@uni-muenster.de

Akshay Mobarsa: akshay.mobarsa@uni-muenster.de

Performed on 11 November 2024

Supervised by : Waleed Esmail

Institute of Nuclear and Particle Physics

University of Münster,D-48149 Münster, Deutschland

Submitted on: 22 December 2024

Contents

1   Introduction

In experimental physics, $\Delta E - E$ detectors, commonly referred to as telescopes, serve as powerful tools for identifying charged particles. These telescopes are composed of pairs of thin and thick surface-barrier detectors arranged in series. The primary purpose of this setup is to provide charged-particle identification. In this experimental configuration, the particle initially traverses the thin detector, where its energy loss is determined. Subsequently, the particle comes to a complete stop in the thick detector, which then measures the energy deposited by the particle. Because there is no fixed α-source in place, a continuous generation of α-rays is achieved by rotating foils positioned between the source and the detector. The rotation of these foils enables the variation of energy loss and deposited energy, facilitating the exploration of this method across a broad energy spectrum.

In this context, we plan to employ the Beth-Bloch formula to identify particles by comparing theoretical and experimental energy values. The detectors utilized in this case are semiconductor detectors.

2   Theory

2.1   Beth-Bloch Formula

A charged particle moving through a substance interacts with the electrons within atoms, leading to ionization or excitation of the atoms. This interaction causes a depletion of energy for the charged particle traversing the material. In theoretical physics, the Bethe-Bloch formula defines the energy loss of a particle moving through matter due to such interactions.

The energy loss dE concerning the distance dx is expressed as:

$$-\frac{dE}{dx} = 2\pi N_a r_e^2 m_e c^2 \rho \frac{Z}{A} \frac{z^2}{\beta^2} \left[\ln \left(\frac{2 m_e \gamma^2 v^2 W_{\max}}{I^2} \right) - 2\beta^2 \right] \tag{1}$$

Avogadro's number, $N_a = 6.022 \times 10^{23} \, \mathrm{mol}^{-1}$, is the number of entities (atoms, molecules, etc.) per mole. The classical electron radius, r_e, represents the size of the electron and has value equal to 2.817×10^{-13} cm, m_e is the mass of the electron and c is a fundamental constant or speed of light. The density of the material is denoted by ρ whereas, Z stands for the atomic number of the material, representing the number of protons in its nucleus. A is the atomic mass of the material, indicating the average mass of its atoms and the charge of the particle is denoted by z. The velocity of the particle as a fraction of the speed of light is given by $\beta(\frac{v}{c})$. The Lorentz factor is represented by γ and the velocity of the particle is denoted by v. $W_{\max}$ signifies the maximum energy transfer in a single collision. Finally, I stands for the mean excitation energy of the material.

Quantity $2\pi N_a r_e^2 m_e c^2 \rho$ has value equal to $0.1535 \, \mathrm{MeV} \ \mathrm{cm}^2/\mathrm{g}$ and mean excitation potential I = 173 eV for silicium absorber.

The Bethe-Bloch formula does not apply effectively to electrons because, in their case, there are additional significant mechanisms of energy loss, notably Bremsstrahlung (energy loss due to acceleration) and pair production. These processes, particularly prominent at higher electron energies, are not considered in the Bethe-Bloch formula, which is primarily designed to address ionization energy loss. Modified equations have been developed to consider the distinctive features of electrons, offering a more precise depiction of their energy loss when interacting with matter.

Correction due to density effect(δ) and shell correction (C) in equation result in the modified equation as:

$$-\frac{dE}{dx} = 2\pi N_a r_e^2 m_e c^2 \rho \frac{Z}{A}\frac{z^2}{\beta^2}\left[\ln\left(\frac{2m_e\gamma^2 v^2 W_{\max}}{I^2}\right) - 2\beta^2 - \delta - 2\frac{C}{Z}\right] \tag{2}$$

In the context of the Bethe-Bloch formula the electric field of an incident particle polarizes atoms in the absorber and the resulting polarization shields distant electrons from the full electric field intensity, reducing their contribution to energy loss. This effect is more pronounced at higher particle energies and varies with material density.

The shell correction accounts for deviations from the assumption of electron stationarity with respect to the incident particle, making equation 1 pertinent when the particle's velocity is comparable or smaller than the orbital velocity of bound electrons. Figure (1) shows the Bethe-Bloch formula curve with and without correction.
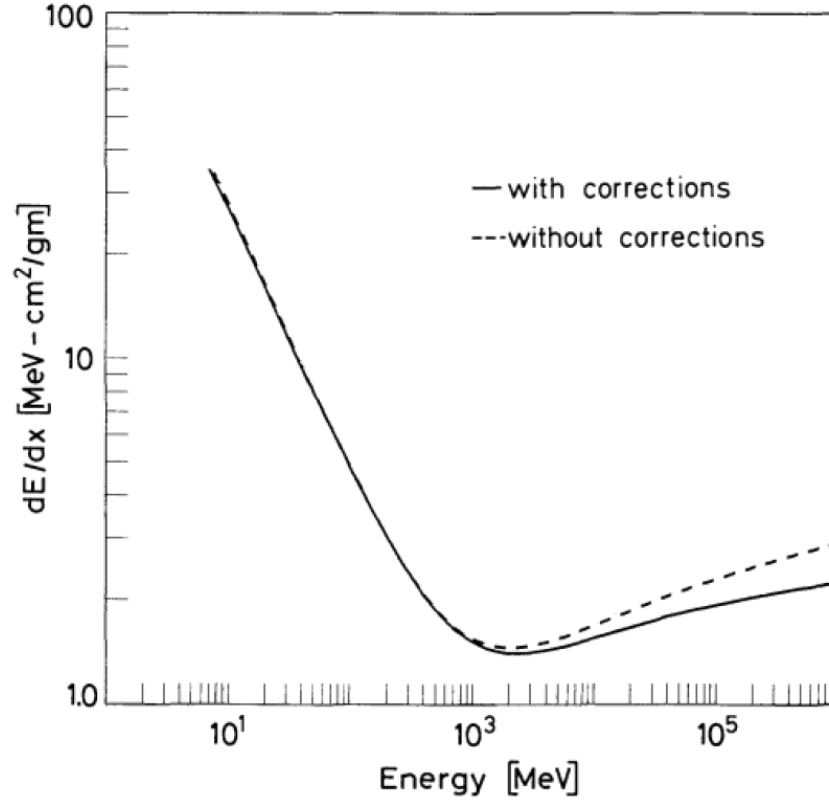

Figure 1: Bethe-Bloch formula with and without correction

The Bethe-Bloch formula describes the energy loss of charged particles as a function of their kinetic energy. At non-relativistic energies, the energy loss per unit length, $-dE/dx$, is primarily dominated by the inverse-square velocity dependence, expressed as $1/\beta^2$, where β is the particle

4

velocity relative to the speed of light. This causes a significant reduction in energy loss as the velocity increases. However, as the particle approaches a velocity $v \approx 0.96c$ (corresponding to $\beta.\gamma \approx 3$, where γ is the Lorentz factor), the energy loss curve reaches a distinct minimum. At this point, particles are referred to as minimally ionizing, and the minimum value of $-dE/dx$ is nearly identical for particles with the same charge. This behavior is clearly illustrated in Figure 2, which shows the energy loss curves for various particles as a function of their kinetic energy.
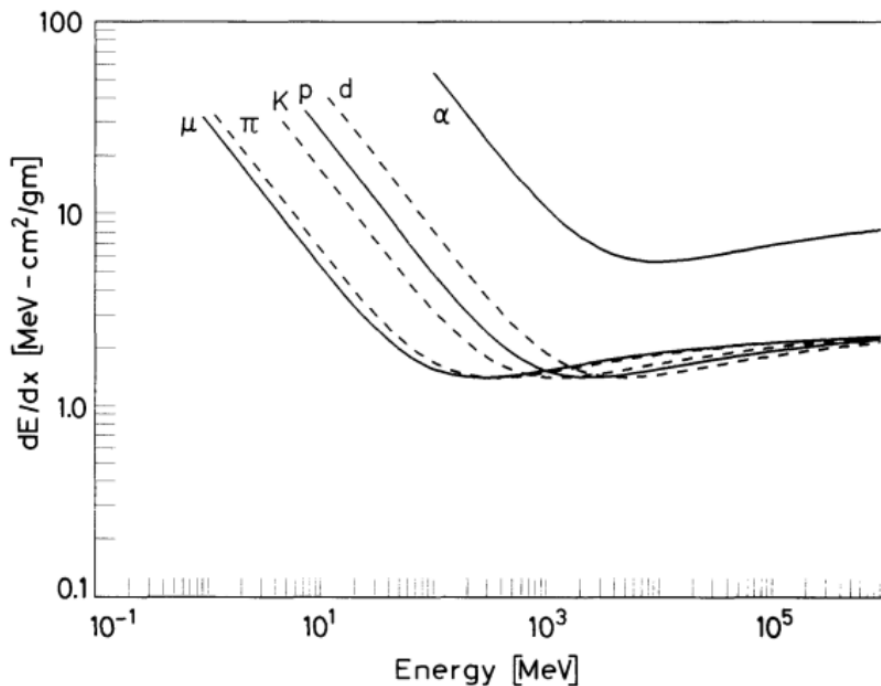

Figure 2: Energy loss of different particles depending on their kinetic energy.

Beyond this minimum, at higher relativistic energies, the energy loss begins to increase logarithmically due to the relativistic increase in particle energy. However, this increase is mitigated by the density effect, which accounts for polarization in the medium, thereby reducing the energy loss at very high energies. The behavior of energy loss varies significantly below the minimum ionization point, as each particle follows a unique curve in this low-energy regime. This distinction is crucial for particle identification since the rate of energy loss becomes dependent on the specific particle type. At extremely low velocities, where the particle's speed becomes smaller than the orbital velocity of the electrons in the absorber material, the energy loss reaches a maximum before dropping sharply. This reduction occurs due to the brief absorption of electrons by the incident particle, which effectively lowers its charge and, consequently, reduces its ability to ionize the medium. The interplay of these intricate effects—velocity dependence, relativistic corrections, and electron absorption—governs the precise nature of the particle's energy loss as it traverses the medium.

5

As a heavy charged particle travels through matter, its kinetic energy decreases, leading to an increase in the energy loss per unit length ($-dE/dx$). This behavior is depicted by the Bragg curve (Figure 3), where energy loss rises sharply toward the end of the particle's path as its velocity decreases. However, shortly before the particle stops, $-dE/dx$ drops due to electron pickup, which reduces the particle's effective charge.
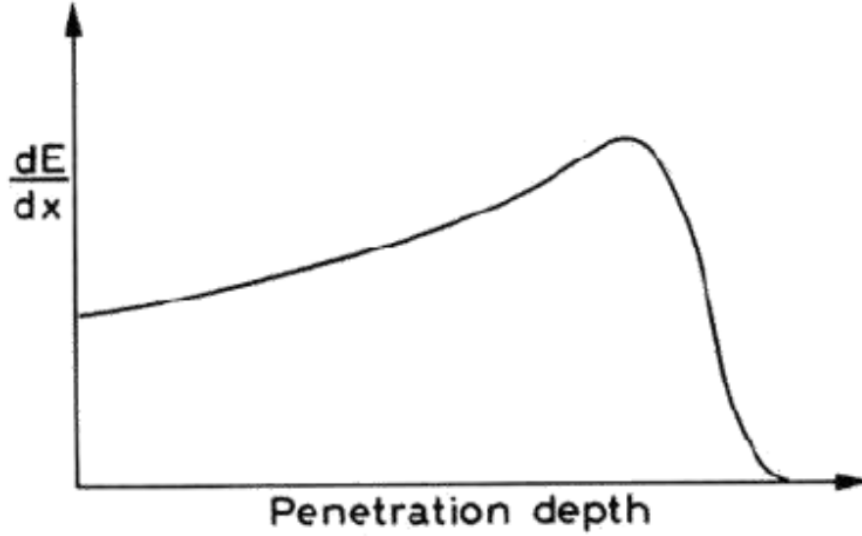

Figure 3: The Bragg curves, Energy loss (dE/dx) of the incident particle as a function of penetration depth

The Bethe-Bloch formula expresses the energy loss per unit path length as a function of the particle's charge and velocity:

$$-\frac{dE}{dx} = z^2 f(\beta) \tag{3}$$

Where z the charge of the incident particle, and β is the velocity of the particle relative to the speed of light.
Since the particle's kinetic energy T is related to its velocity through $T = (\gamma - 1)Mc^2$, where M is the particle's mass and γ is the Lorentz factor, the Bethe-Bloch formula can also be expressed as:

$$-\frac{dE}{dx} = z^2 f'\left(\frac{T}{M}\right) \tag{4}$$

The range of a particle is defined as the total distance it travels in a medium before it loses all its energy due to continuous energy loss. For identical particles with the same initial energy traveling through the same material, the range is expected to be well-defined under ideal conditions. However, due to statistical variations in the number of collisions that particles experience in the medium, the energy loss is not uniform, resulting in a distribution of ranges known as range straggling. Experimentally, the range is determined by measuring the transmission of a particle

beam as a function of absorber thickness. As shown in Figure 4, the transmission curve initially remains high when the absorber thickness is small, meaning most particles pass through the material. As the thickness increases, the transmission drops progressively but does not immediately fall to zero. This gradual drop reflects the statistical nature of energy loss, where particles do not all stop at the same point.
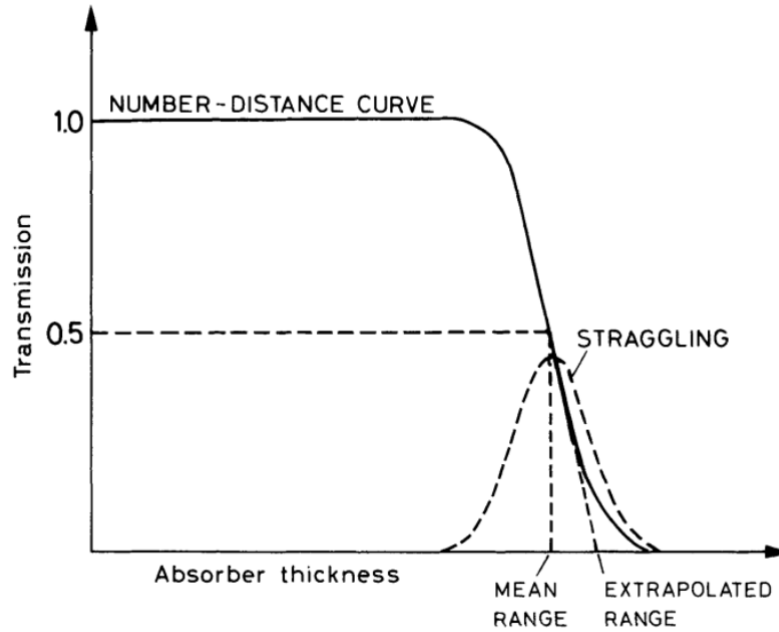

Figure 4: Transmission as a function of absorber thickness (Gaussian distribution)

The distribution of ranges can be approximated as Gaussian, with the mean range corresponding to the central value of the distribution. In Figure 4, the center of the sloping curve represents the mean range, where about half of the particles are absorbed. To determine the practical or extrapolated range, the tangent at the midpoint of the sloping curve is extended to the zero transmission level. This statistical behavior highlights the limitations of assuming a perfectly continuous energy loss and demonstrates the effects of energy loss fluctuations in matter. The concept of range straggling and its measurement are critical in fields like radiation dosimetry and material analysis, where precise energy deposition must be accounted for.

2.2 Landau Distribution

The Landau distribution offers a probabilistic account of the variations in energy loss encountered by nuclear particles during their interactions with matter.It is influenced by the characteristics of the material through which the particle is passing. Different types of absorbers, with varying densities and compositions, can indeed result in different Landau distribution curves. In case of thin absorbers number of collision is comparatively small and central limit theorem would not be applicable here, energy loss distribution for thin absorbers is shown in figure 5.
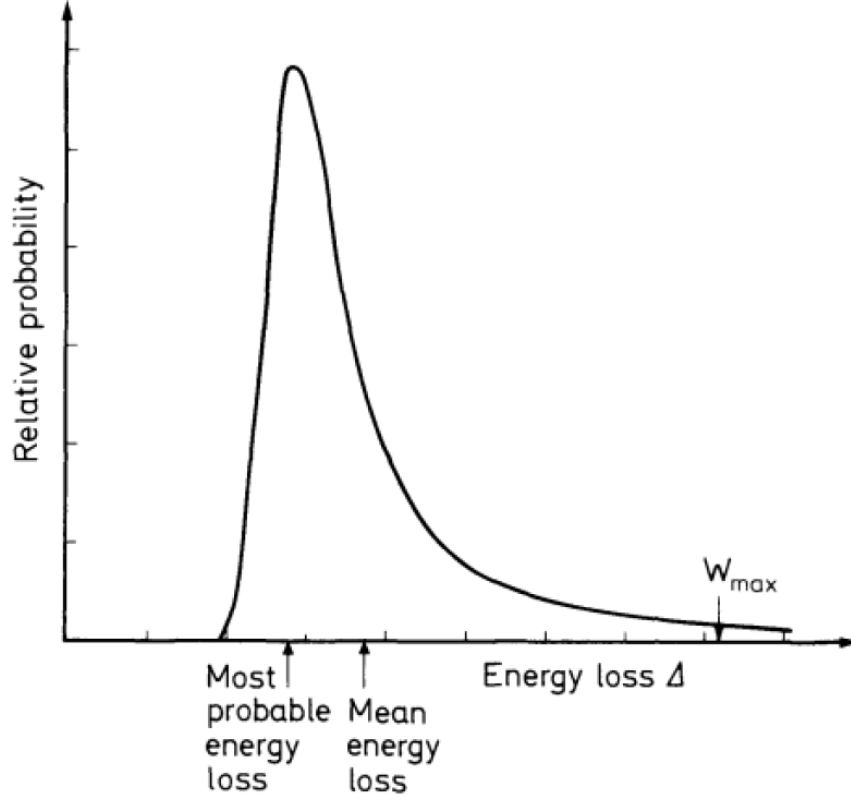
Figure 5: Typical energy loss distribution for thin absorbers

Equation (2) provides the maximum energy transfer $W_{\max}$ for heavy particles. However, for electrons, only up to half of their energy can be transferred. Furthermore, the potential for significant energy loss due to Bremsstrahlung exists, even though such events are infrequent. The distribution depicted in figure-2 exhibits a prolonged tail at higher energies, creating an asymmetric shape which means the mean energy loss does not corresponds to the peak position and may slightly offset.

2.3 $\alpha -$ Radiation

In isotopes that emit alpha particles, the mass number decreases by four due to the loss of 4 nucleons, and the atomic number decreases by two due to the loss of 2 protons. If we consider the original isotope as X and the resulting daughter isotope as Y, the general mechanism can be expressed by the following equation.

$$\ ^{A}_{Z}X \rightarrow\ ^{A-4}_{Z-2}Y +\ ^{4}_{2}\alpha \tag{5}$$

Alpha decay occurs due to the Coulomb repulsion between the alpha particle and the remaining nucleus. Both entities possess a positive electric charge, but the nuclear force acts as a balancing

8

factor, preventing uncontrolled separation, Figure (6) shows the potential energy of the $\alpha-$ particle as a function of its distance R from center of the nucleus. Classically, alpha decay is considered forbidden because the decay energy ($Q \approx 5\,\text{MeV}$ for an alpha particle) is smaller than the Coulomb barrier of the nucleus:

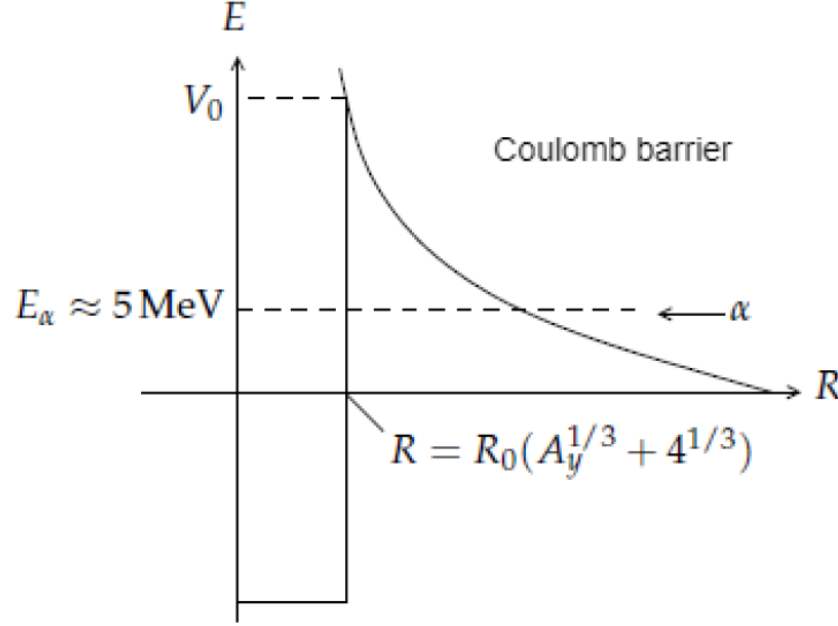$$V_0 \approx \frac{\alpha \hbar c^2 Z_1 Z_2}{R} \approx 30\,\text{MeV}. \tag{6}$$

Figure 6: Illustration depicting the Coulomb barrier of the daughter nucleus in the context of α-decay.

The $\alpha-$ particle confined within the potential barrier needs to undergo tunneling, and the likelihood of tunneling is expressed by the probability.

$$T = e^{-2G} \quad \text{Where} \quad G = \frac{1}{\hbar} \int_R^{r_1} dr \sqrt{2m(|E - V|)dr} \tag{7}$$

In this experimental setup, the alpha source used is ^{241}Am, playing a role in a complex decay scheme that encompasses more than 40 excited states of ^{237}Np. The primary transitions involves the emission of α-particles with energies of 5485.56 keV (84.45%) and 5442.86 keV (13.23%). Although these represent the most probable scenarios, a detailed summary of all potential outcomes is provided in the table shown in Table 1.

Table 1: Energy values and probabilities of α emissions of the isotope ^{241}Am.

Transition	Energy (keV)	Probability (%)
$\alpha_{0,36}$	4757.41 (16)	0.00004 (3)
$\alpha_{0,34}$	4800.68 (16)	0.00086
$\alpha_{0,33}$	4834.16 (13)	0.0007
$\alpha_{0,32}$	4889.0 (2)	
$\alpha_{0,30}$	4956.1 (3)	
$\alpha_{0,29}$	4961.7 (11)	
$\alpha_{0,28}$	4963.64 (20)	
$\alpha_{0,27}$	5007.59 (20)	0.0001
$\alpha_{0,25}$	5055.35 (14)	
$\alpha_{0,24}$	5066.23 (17)	0.00011
$\alpha_{0,23}$	5092.06 (13)	0.0004
$\alpha_{0,22}$	5099.10 (13)	0.0004
$\alpha_{0,21}$	5106.72 (16)	
$\alpha_{0,20}$	5117.21 (20)	0.0004
$\alpha_{0,19}$	5133.0 (4)	
$\alpha_{0,18}$	5155.16 (13)	0.0007
$\alpha_{0,17}$	5179.35 (13)	0.0005
$\alpha_{0,16}$	5181.65 (13)	0.0009
$\alpha_{0,15}$	5190.4 (2)	0.0006
$\alpha_{0,14}$	5217.28 (13)	
$\alpha_{0,13}$	5225.85 (13)	0.0013
$\alpha_{0,12}$	5232.6 (3)	
$\alpha_{0,11}$	5244.12 (10)	0.0022 (3)
$\alpha_{0,10}$	5281.02 (14)	0.0005
$\alpha_{0,9}$	5321.91 (13)	0.014 (3)
$\alpha_{0,8}$	5388.26 (13)	1.66 (3)
$\alpha_{0,7}$	5416.27 (16)	0.01
$\alpha_{0,6}$	5422.86 (12)	13.23 (10)
$\alpha_{0,5}$	5469.47 (12)	0.04
$\alpha_{0,4}$	5485.56 (12)	84.45 (10)
$\alpha_{0,3}$	5511.47 (12)	0.23 (1)
$\alpha_{0,0}$	5544.11 (12)	0.38 (1)

2.4 Semiconductor detector

A semiconductor detector is a radiation-detecting device that employs semiconductor materials to identify ionizing radiation, including alpha particles, beta particles, and gamma rays. These

detectors capitalize on the capability of semiconductors to generate electrical signals when ionizing radiation interacts with the semiconductor material. In this experiment we will be using silicon semiconductor.

In a crystalline solid, atoms are arranged in a regular lattice structure. Electrons within this structure occupy quasi-continuous energy bands, limiting their energy levels. In between there are regions of forbidden energies also called the band gap denoted by E_g, depending upon the size of the band gap a material can be classified as a semiconductor or insulator. Here, our interest lies in the conduction band(CB) and valence band(VB), the valence band comprises of outer electrons that are bound in the crystal and in silicon these are the electrons involved in the covalent bond while the electrons in the conduction band are freely movable and contribute to the electrical conductivity of a material. Figure 7 gives the schematic representation of the band model.
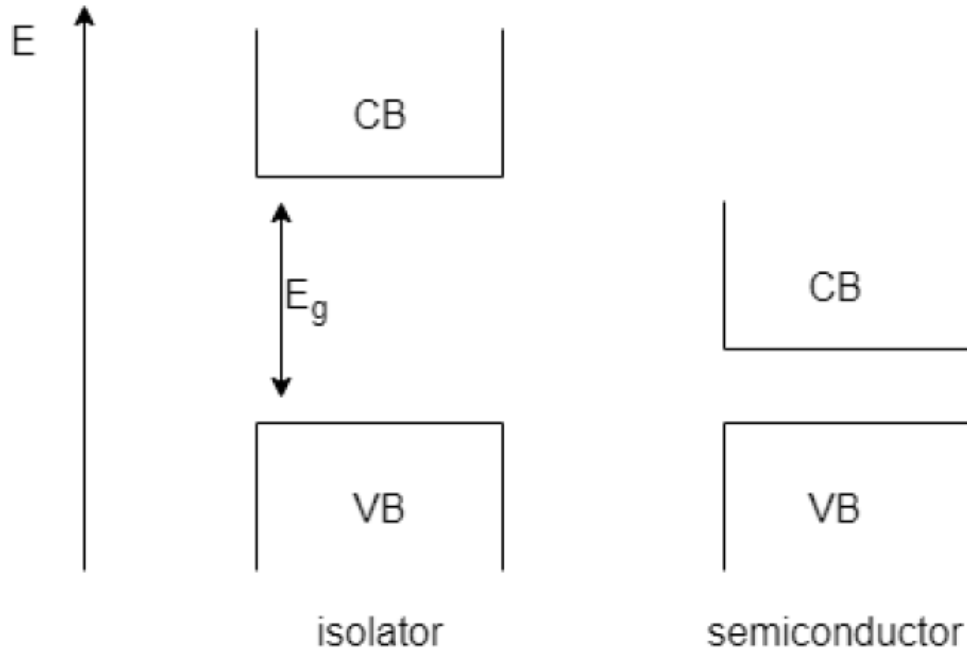

Figure 7: Band model showing VB,CB and Band gap

In an intrinsic semiconductor, the number of electrons in the CB and holes in the VB band is the same, and it is practically not possible to produce such a semiconductor. So, the intrinsic semiconductors are doped, i.e. insertion of foreign atoms in crystal lattice, depending upon the type of the atoms used for doping semiconductors are classified as P-type and N-type.

2.4.1   P-type Semiconductor

Trivalent atoms, such as boron, are employed for doping in this context. Due to boron's deficiency of one valence electron required for a complete covalent bond with silicon, a hole is formed. The

11

process of p-doping introduces acceptor levels near the upper limit of the valence band, as depicted in the figure (8).

2.4.2 N-type Semiconductor

A pentavalent impurity, in the form of phosphorus, is incorporated into the crystal. Since phosphorus possesses five valence electrons, one of these electrons remains unbound and can be readily elevated to the conduction band with minimal energy input. In summary due to n-doping of silicon semiconductor there is and extra electron and creation of donator level near to the CB and due to p-doping there is a extra hole in VB and acceptor level is created.A schematic representation of this is shown in the figure (9).
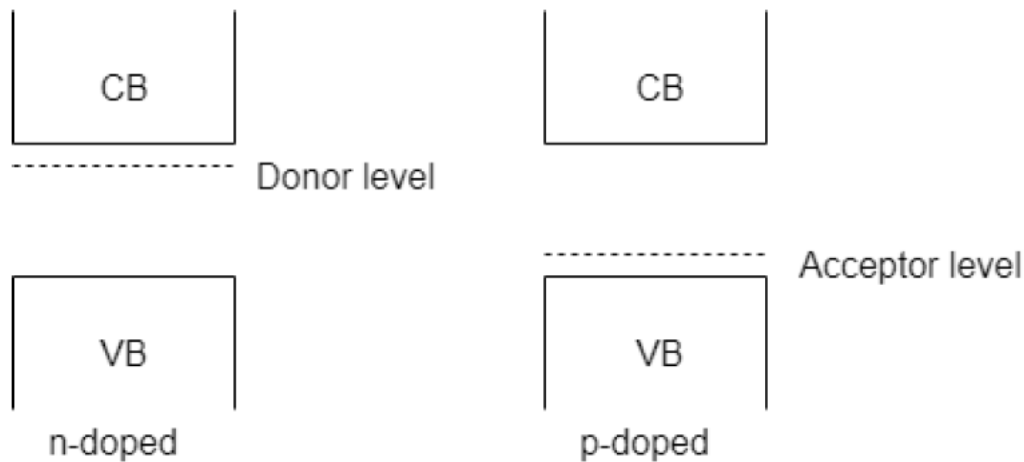

Figure 8: N and P doped Semiconductor

2.4.3 P-N jn and its Characteristics

A P-N junction is created when a P-type semiconductor is in contact with an N-type semiconductor.In the N-region, the concentration of conduction electrons exceeds that in the P-region. When the two regions come into contact, the primary charge carriers move from the region with a higher concentration to the one with a lower concentration. Electrons migrate from the N-region to the P-region, where they unite with holes. This process results in the presence of immobile positive charges in the N-region, stemming from the stationary doping atoms. Additionally, holes travel from the P-region to the N-region, leaving behind stationary negative charges in the P-region. Figure (9) gives schematic representation of the same.
These fixed charges create an electric field in the transition region, opposing the diffusion of charge carriers and establishing a state of equilibrium. The area containing these immobile charges is termed the depletion region, and its dimensions are influenced by the dopant type and the intrinsic density of charge carriers.
When a positive voltage is applied to the P-type semiconductor and a negative voltage to the N-type semiconductor, the P-N junction is considered to be in forward bias. In this scenario, the

Figure 9: On Left P-N junction showing direction of electron and hole diffusion, On left formation of depletion region due to remaining stationary charges

depletion region narrows, and the barrier potential decreases. This reduction in barrier potential facilitates the smooth flow of majority charge carriers. Consequently, current initiates and flows through the diode, making it conductive. The current-versus-voltage graph illustrates an exponential growth, as depicted in the figure (10).

In the case of reverse bias, where negative voltage is applied to the P-type semiconductor and positive voltage to the N-type semiconductor, the P-N junction undergoes specific changes. Notably, the depletion region widens, leading to an elevation in the barrier potential. This increased depletion region acts as a barrier, impeding the flow of majority charge carriers and resulting in minimal current. Consequently, the diode, when subjected to reverse bias, assumes a non-conductive state.

The current-versus-voltage graph during reverse bias typically depicts a low, nearly negligible reverse current. This low current persists until a certain reverse breakdown voltage is attained. Beyond this critical point, there is a sudden and substantial increase in current, often indicating breakdown. The characteristics of a PN junction diode under reverse bias conditions are visually represented in the accompanying figure.
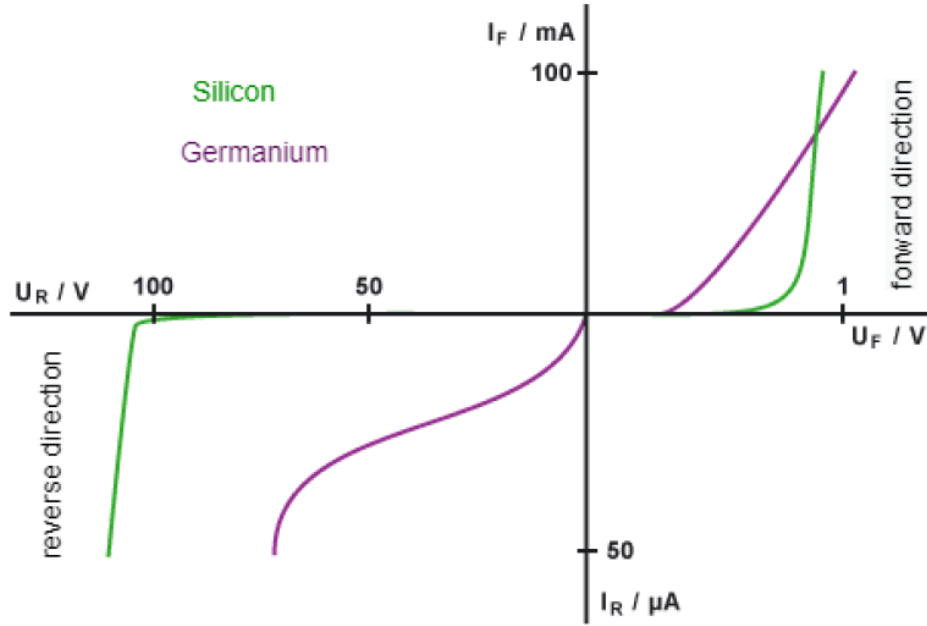
Figure 10: Characteristic curve PN Jn diode made of Silicon and Germanium

3 Experimental Setup

The experimental arrangement presented in Figure (11) utilizes ^{241}Am as the radiation source, housed within a vacuum chamber. Within this chamber, there are two detectors namely, the thick and thin detectors alongside foils. The signals from both detectors undergo a sequence where they are initially directed to preamplifier and subsequently to main amplifiers. Simultaneously, the signal from the thick detector (E) is sent to a discriminator, allowing only signals above a specific level to pass through. The output from the discriminator is then routed to a timer, generating a square wave signal that serves as a gate for the ADC. This gate specifies the time duration during which the ADC is capable of receiving signals and only coincident events are recorded by the ΔE detector.
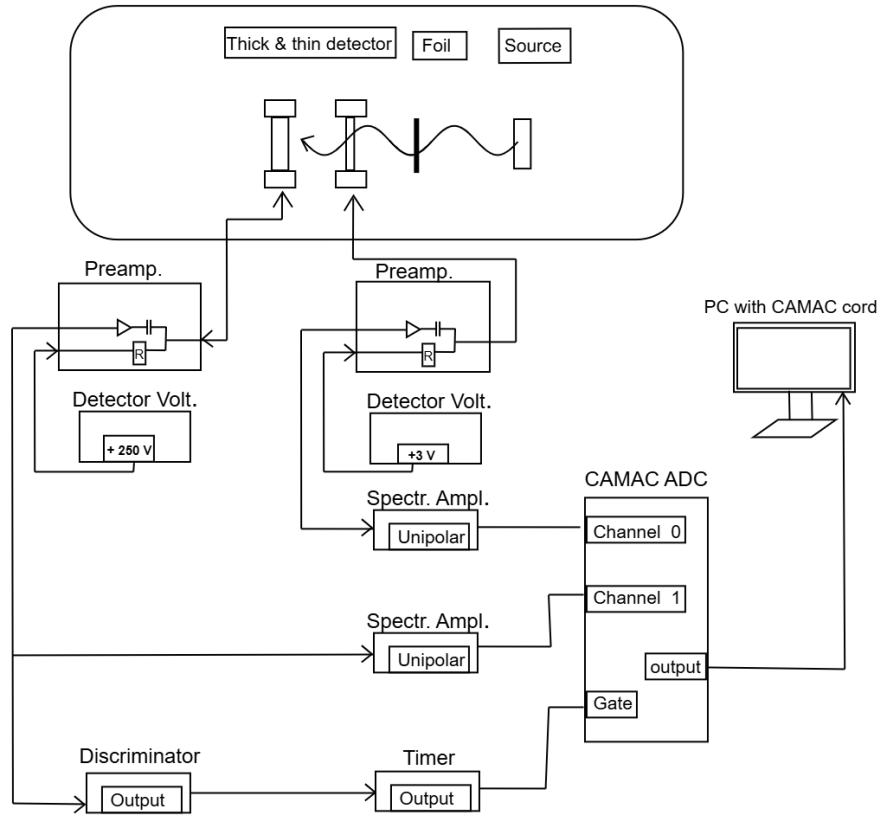
Figure 11: Experimental setup with ^{241}Am as the radiation source in a vacuum chamber, featuring thick and thin detectors. Signals are processed via preamplifiers, amplifiers, and a discriminator, recording coincident events with the ΔE detector.

4   Result and Analysis

4.1   Calibration of the E-detector

To calibrate the E-detector, the ΔE is first rotated out of the α-particle beam path, and the foil holder is completely retracted to ensure no interference with measurement. The α-spectrum of ^{241}Am is then recorded using E-detector, ensuring a sufficient number of events are collected to clearly resolve the spectral features. The spectrum is analyzed to identify the channel with the maximum count rate, which corresponds to the peak of the α-particles emitted by ^{241}Am.
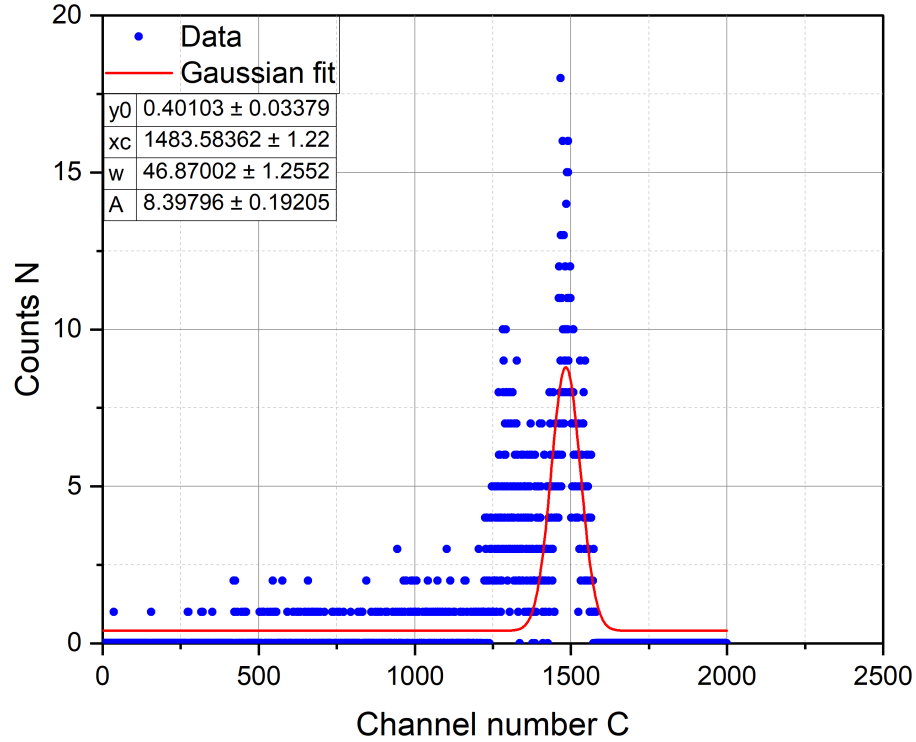

Figure 12: Histogram of Counts N vs Channel Number C with Gaussian Fit for E-detector

The histogram shown in figure 12 illustrates the distribution of counts (N) as a function of channel number (C). A Gaussian fit (red curve) has been applied to the data, which effectively models the observed peak in the histogram. This peak indicates a region of high concentration, centered around the channel number $C = 1483.58 \pm 1.22$, the fitted parameter Xc (the peak center). The amplitude of the peak is $A = 8.39 \pm 0.19$, representing the maximum number of counts observed at the peak.

16

Figure 12 clearly shows two peaks; however, only the dominant peak is analyzed and fitted using the Gaussian fit function. This dominant peak corresponds to the most probable α- particle transition, which has an energy of 5485.56 keV. The channel number is assumed to have a linear relationship with the energy E, allowing the E-detector to be determined. Using the reference point for the center of the dominant peak at $Xc = 1483.58 \pm 1.22$, the calibration is calculated accordingly.

$$E_{cal} = \frac{\alpha_{0,2}}{Xc} = 3.6975 \pm 0.003 \, \text{keV} \tag{8}$$

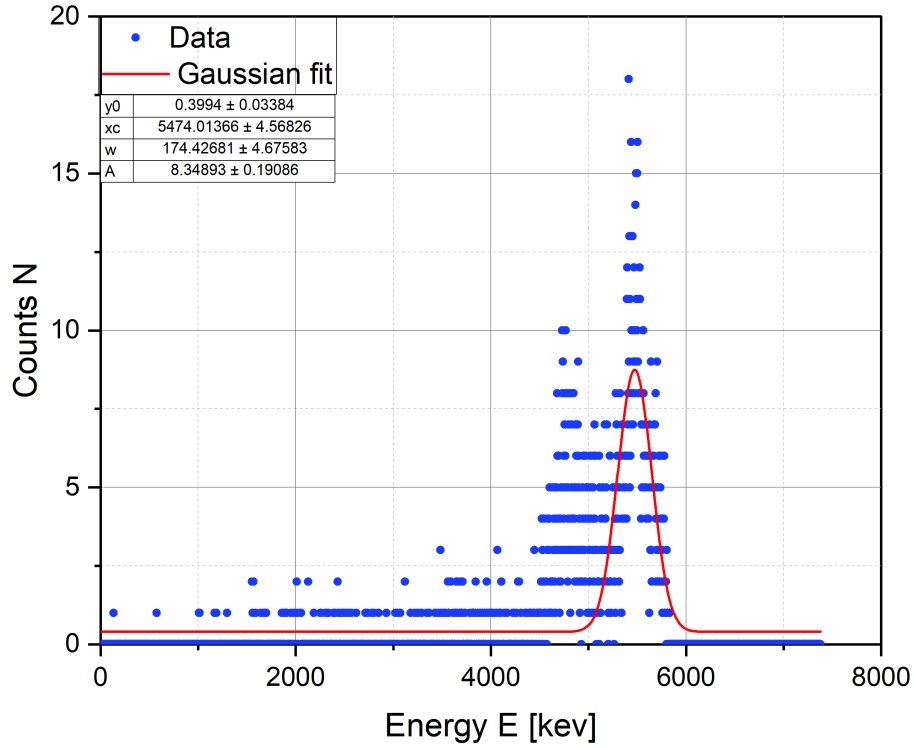|	
y0	0.3994 ± 0.03384
xc	5474.01366 ± 4.56826
w	174.42681 ± 4.67583
A	8.34893 ± 0.19086

Figure 13: Histogram of Counts N vs Energy E with Gaussian Fit for E-detector

The calibrated data for the E-detector shows a clear relationship between energy and channel numbers. The plotted graph illustrates the calibrated energy spectrum of the E-detector alongside the total counts. The dominant peak in the spectrum represents the energy of the α- particle, which closely matches the theoretical value of 5485.56 keV. Any slight difference observed is likely due to statistical fluctuations in the energy distribution, which can be attributed to the inherent resolution of the detector or minor variations in the measurement process. This calibration

17

demonstrates the accuracy of the detector and confirms that the Gaussian fitting method effectively identifies the key spectral features.

4.2 Calibration and determination of the thickness of the ΔE-detector

Now, the ΔE-detector is reintroduced into the beam path to facilitate calibration and to determined its thickness. The α-particle of ^{241}Am is recorded for both detectors, and measured counts N are plotted against the channel number C. The energy deposited in the ΔE-detector is calculated as the difference between the energy of α-peak obtained during the initial measurement and the energy recorded by the E-detector. According to the principle of energy conservation, this value corresponds to the peak energy in the ΔE-detector. For simplicity, the channel number "0" is assumed to represent $E = 0$.
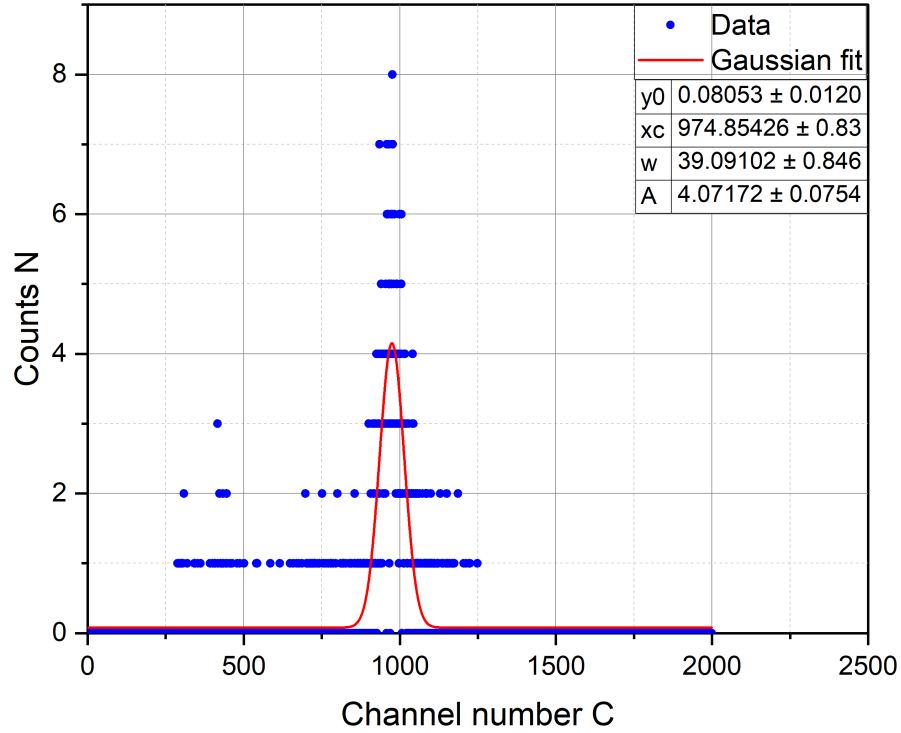

Figure 14: Histogram of Counts N vs Channel number C with Gaussian Fit. Here, the measured counts are from E and ΔE detectors

The measured data is fitted with a Gaussian function, revealing a distinct peak at the channel number C, with the peak center located at $Xc = 974.85 \pm 0.83$. This peak serves as a critical reference point for the calibration of the ΔE-detector. The mathematical expression is shown as:

$$\Delta E_{cal} = \frac{\alpha_{0,2}}{Xc} = 5.627 \pm 0.004\,\mathrm{keV} \tag{9}$$
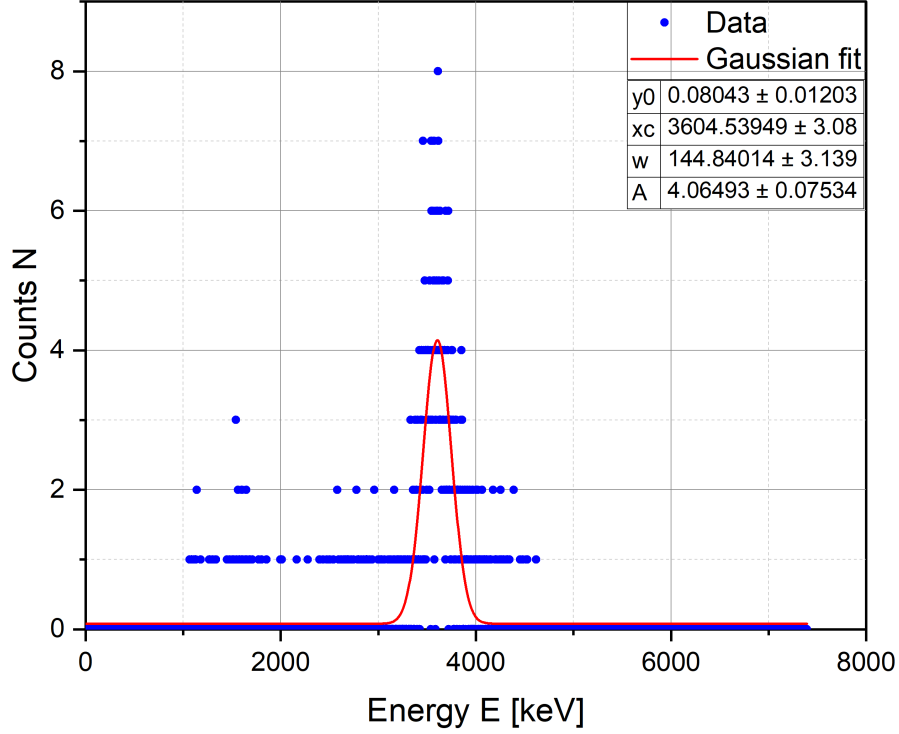

Figure 15: Histogram of Counts N of E and ΔE-detector vs calibrated energy E with Gaussian fit.

Figure 15 presents the plotted data of counts N versus calibrated energy E. The dominant peak in the data is fitted using a Gaussian function, yielding a peak center (Xc) at 3604.53 ± 3.08 keV, which corresponds to the energy detected by the ΔE-detector. Similarly, Figure 13 shows the energy detected by the E-detector, with the peak centered at 5474.01 ± 4.56 keV.
The difference between the energies at the centers of the peaks in Figures 13 and 15 represents the energy deposited in the ΔE-detector. This calculation accounts for the energy lost as particles traverse the ΔE-detector. By subtracting the energy detected by the ΔE-detector ($3604.53 keV$) from the energy detected by the E-detector ($5474.01 keV$) the deposited energy can be calculated:

$$\Delta E = 1869.48 \pm 5.50\,\mathrm{keV} \tag{10}$$

19

The deposited energy in the ΔE-detector is calculated using Equation (10). This value is then used to determine the thickness of the ΔE-detector by using the energy loss of alpha particles in silicon, expressed as $\frac{dE}{dx}$, expressed as:

$$\frac{dE}{dx} = \frac{\Delta E}{x} \tag{11}$$

Figure 15 illustrates the detected energy in the ΔE-detector. Since the energy loss of alpha particles in silicon corresponds to the incoming alpha particle energy, which is 5485.56 keV, the tabulated values of energy loss must be interpolated between 3500 keV and 5500 keV. The interpolation is performed using the following equation:

$$\frac{dE}{dx} = y = y_0 + (x - x_0).\frac{(y_1 - y_0)}{(x_1 - x_0)} = 171.99\,\text{keV}/\mu m \tag{12}$$

Using equation (13), the thickness of the ΔE-detector (x) is determined by rearranging the equation. The necessary values for this calculation are obtained from Equations (10) and (12). By substituting these values into the rearranged equation, the thickness of the ΔE-detector can be calculated as:

$$x = \frac{\Delta E}{\frac{dE}{dx}} = 10.86 \pm 0.031\,\mu m \tag{13}$$

4.3 Determination of the thickness of the 3 foils using the E-detector

To determine the thickness of the three Mylar foils, the ΔE-detector was rotated out of the beam path to allow an unobstructed measurement. The foil holder was inserted into the measurement setup so that the foil was positioned vertically at an angle of 0° between the source and the E-detector. The α-spectrum from ^{241}Am was then recorded. This procedure was repeated for the second and third foils by successively placing each foil into the holder and measuring the corresponding α-spectrum. The recorded spectra for all three foils were superimposed and plotted against energy E, which is shown in figure 16.

This histogram illustrates the energy loss of α-particles due to the Mylar foils placed between the source and the E-detector. The peaks represent the detected energy after passing through each foil. It can be observed that as we progress from the black peak (first foil) to the blue peak (third foil), the detected energy decreases due to energy being deposited in the Mylar foils. The energy deposited in the first foil is calculated as the difference between the energy measured by the E-detector without a foil (refer to Fig. 13) and the position of the first peak (black) in this histogram. For the second foil, the energy loss is determined by subtracting the position of the first peak (black) from the second peak (green), as shown in Figure 16. Similarly, the energy loss in the third foil is calculated as the difference between the position of the second peak (green) and the third peak (blue), also shown in Figure 16.

The deposited energy values for each foil are summarized in Table 2. By referencing the energy loss data of α-particles in Mylar and interpolating these values using equation 12, the exact energy loss for each foil was determined. Subsequently, the thickness of each Mylar foil was calculated using equation 13, and the results are presented in Table 2.

The tabulated results indicate that as the energy deposited (ΔE) by the α-particles increases with successive foils, the corresponding energy loss per unit thickness (dE/dx) also increases. This
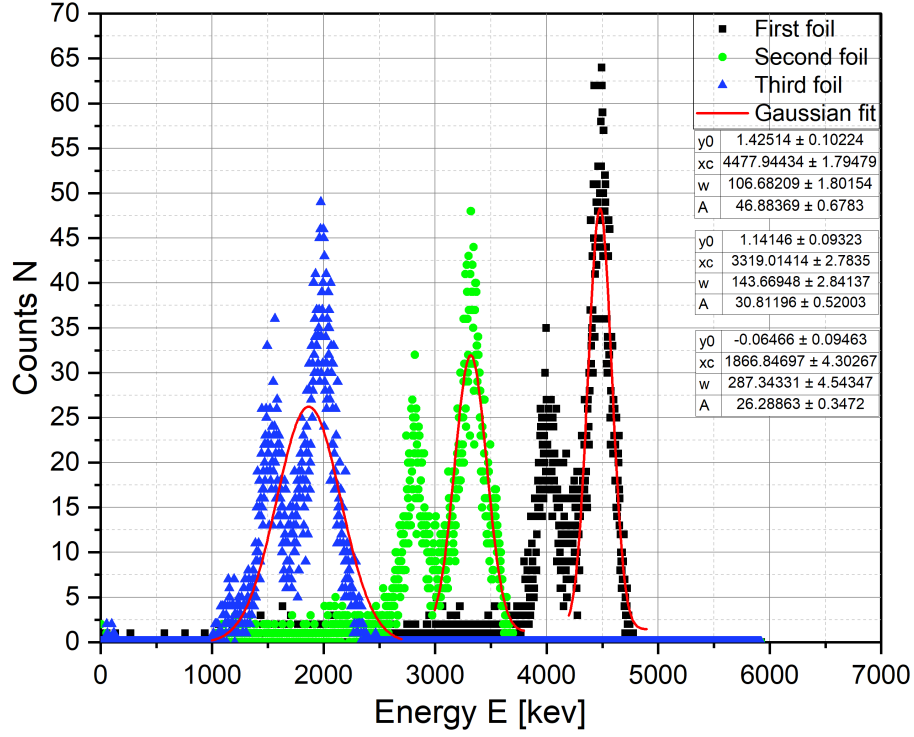
20

Figure 16: Histogram of counts N of the E-detector with three Mylar foil vs calibrated energy E with Gaussian fit.

Foils	Energy deposited ΔE [keV]	Energy loss dE/dx [keV/μm]	Thickness x [μm]
1	996.07	118.828	8.3824
2	1158.93	140.539	8.2463
3	1452.17	180.753	8.034

Table 2: Energy deposited, energy loss, and thickness data for different foils.

trend suggests that the energy deposited into the Mylar foils is accumulating, resulting in greater interactions as the α-particles lose energy while passing through each additional foil. Interestingly, the thickness (x) values of the three Mylar foils are close to each other, with a slight variation.

4.4 Determination of the energy loss in the ΔE-detector at different energies

In this part of the experiment, the ΔE-detector was repositioned into the beam path to measure the energy spectrum under varying conditions. The CAMAC system was employed to detect and record coincident events, ensuring that only those signals occurring simultaneously in both detectors were considered valid. Initially, the α-spectrum was recorded without any foils to establish a baseline. Subsequently, the first foil was inserted into the beam path, and measurements were taken as the foil holder was rotated incrementally from 0° to 60° in 15° steps. Once this process was completed, the second foil was introduced. Similar angular rotations and measurements were conducted, spanning the range from 0° to 60°. Finally, the third foil was inserted, and the energy spectrum was recorded at the angles 0° and 15°, ensuring sufficient data acquisition without pausing between the angular steps.

The recorded spectrum revealed a broad energy distribution corresponding to 1-5 MeV, with a noticeable decrease in the count rate as more foils were added. This reduction can be attributed to the increasing energy loss of the α-particles as they traverse the foils. As the number of foils increases, the α-particles lose more energy, leading to reduced velocity. This slowing down decreases the probability of coincident detection events since the likelihood of simultaneous signals in both detectors is diminished.
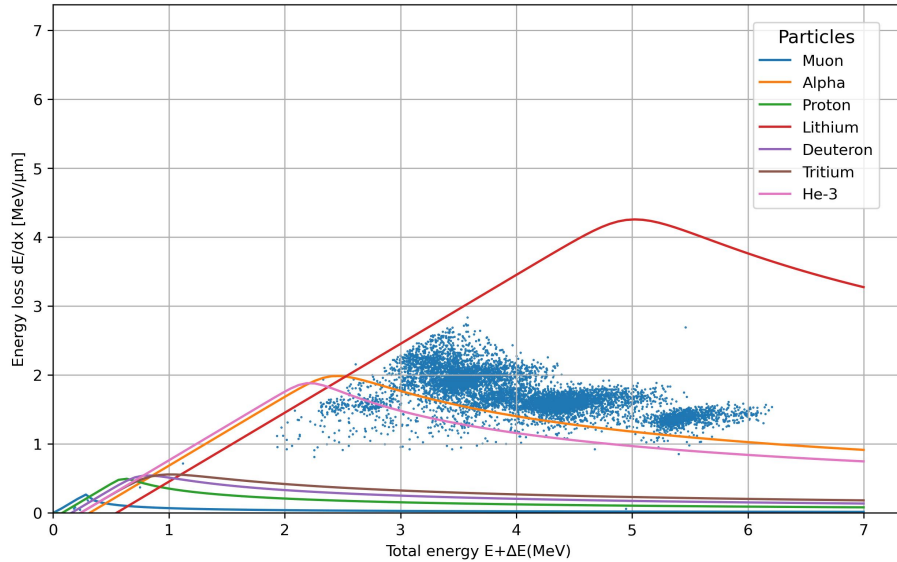

Figure 17: Histogram of energy loss (dE/dx) against total energy $E + \Delta E$. The theoretically calculated curves for various particles are superimposed onto the experimental data.

Figure 17 illustrates the energy loss (dE/dx) plotted against the total energy $(E + \Delta E)$. Theoretically predicted curves for protons, deuterons, tritium, helium-3, alpha particles, and lithium were calculated using the Bethe-Bloch formula (Eq.2), with the necessary parameters provided in the appendix. These theoretical curves were then superimposed onto the measured

experimental data to allow comparison. The plot reveals that the α-particles (orange curve) closely match the observed data, demonstrating a good fit. Although the helium-3 particles (pink curve) show a similar trend to the alpha particles, their energy loss values are slightly lower. On the other hand, the fit for lithium particles (red curve) deviates significantly, showing much higher energy loss, particularly at increased energy values. The remaining particles—protons, deuterons, and tritium—exhibit lower energy loss compared to the alpha particles, as seen in their corresponding curves.

The primary objective of this part of the experiment was to identify the α-particles among the detected signals and compare their energy loss characteristics with other particles. The results, supported by the theoretical predictions using the Bethe-Bloch formula, validate the distinction of α-particles and emphasize their higher stopping power in the medium compared to other particle types.
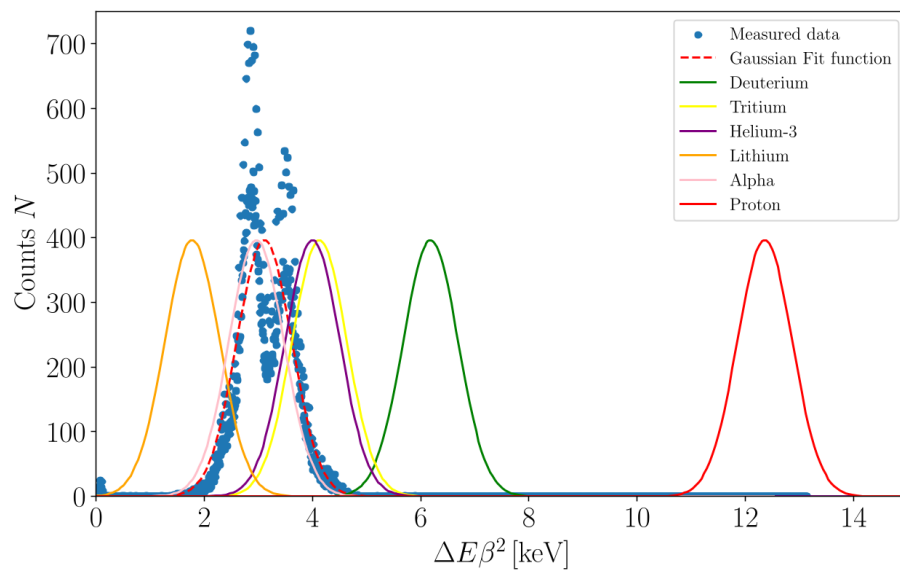

Figure 18: Histogram of counts N against $\Delta E \beta^2$ with Gaussian fit function. The theoretically calculated curves for certain particles with same hight of Gaussian line in various color.

"Why is such a diagram useful ?"

In this figure 18, charged particles of various types (e.g., protons, deuterons, tritons, helium-3 ions, alpha particles, and lithium ions) are identified by measuring their energy loss, ΔE, and velocity, expressed through $\beta = v/c$. Plotting the number of events against the product $\Delta E.\beta^2$ is especially useful because it clusters each particle species at a distinct position on the horizontal axis. This happens due to the different mass and charge of each ion, which result in characteristic stopping powers and energy-deposition patterns in the detector. By normalizing the energy loss with β^2, one effectively accounts for how rapidly the particle is moving and how much energy it transfers per unit distance, producing well-separated peaks for each species. Comparing the measured data points with theoretical Gaussian-like peaks for each ion makes it straightforward to identify and count each particle type in a mixed beam. Such particle identification is essential

for determining reaction products, cross-sections, and other key parameters in nuclear and particle physics experiments, and the clarity of this $\Delta E.\beta^2$ plot ensures reliable discrimination among different ions.

5   Conclusion

This experiment utilized the ΔE-E telescope setup to achieve precise particle identification and material characterization, confirming its reliability and consistency with theoretical models. By systematically calibrating the E and ΔE detectors and performing a series of measurements, we obtained critical insights into the energy loss and deposition characteristics of ^{241}Am α-particle, as well as the structural properties of the materials under investigation.

First, The E-detector was calibrated by first removing the ΔE-detector from the α-particle beam path to ensure unimpeded measurements. The spectrum of the ^{241}Am source was recorded, and the dominant $\alpha_{0,2}$ peak at 5474.01 ± 4.56 keV was identified (Figure 13). A Gaussian fit to the spectral data provided the peak position in terms of channel number, enabling the derivation of a linear energy-channel relationship, $E_{Cal} = 3.6975 \pm 0.003$ keV. Second, the ΔE-detector was introduced into the beam path to measure energy deposited in the thin detector. By comparing the spectra (Figures 13 and 15) with and without the ΔE-detector, the deposited energy was determined as $\Delta E = (1869.48 \pm 5.50)$ keV (Eq.10). Using the interpolated energy loss rate of 171.99 keV/μm for silicon (Eq.12), the thickness of the ΔE-detector was calculated as $x = 10.86 \pm 0.031\ \mu m$.

Moreover, the thicknesses of three Mylar foils were measured by inserting the foils sequentially into the α-particle beam path. The energy spectra recorded for each foil were analyzed using Gaussian fits to identify the energy deposited by the α-particles. The deposited energy values for the first, second, and third foils were $\Delta E_1 = 996.07$ keV, $\Delta E_2 = 1158.93$ keV, and $\Delta E_3 = 1452.17$ keV, respectively (Figure 16). By applying the energy loss rate for Mylar, the foil thicknesses were determined as

- $x_1 = 8.3824\ \mu m$,

- $x_2 = 8.2463\ \mu m$, and

- $x_3 = 8.034\ \mu m$, for reference (Table 2)

Lastly, the energy loss dE/dx in the ΔE-detector was measured at various particle energies by inserting Mylar foils at different angles ($0°$ to $60°$). The recorded spectra showed a decreasing count rate as more foils were added, reflecting the increased energy loss by the α-particles (Figure 17). The experimentally observed dE/dx values closely matched the theoretical predictions from the Bethe-Bloch formula (Eq.2) for α-particles, as evidenced by the alignment of the experimental data with the α-particle curve in Figure 17.

The $\Delta E.\beta^2$ plot provided an additional layer of particle identification by clustering different species at distinct positions based on their mass and charge. Normalizing energy loss with β^2 accounted for particle velocity, producing well-separated peaks for each species, including protons, deuterons, tritons, helium-3, lithium, and α-particle. The clarity of this Figure 18 ensured reliable discrimination among particle types, enabling straight forward identification and counting in a mixed beam.

This experiment provided valuable hands-on experience in detector calibration, energy loss analysis, and material characterization. It highlighted the importance of integrating experimental observations with theoretical frameworks to understand particle behavior in complex systems.
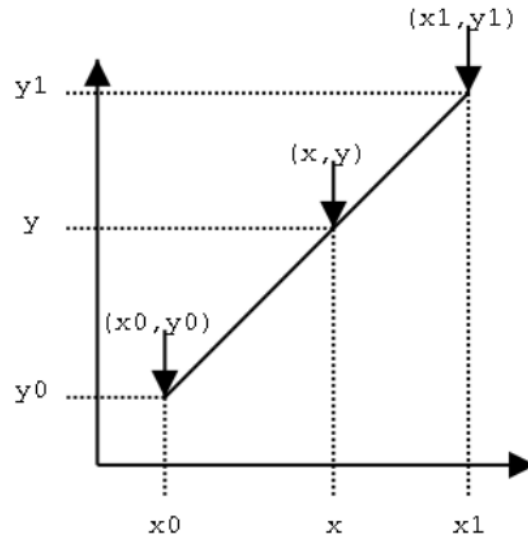
6 References

[1] Preparation material: Particle identification with the ΔE-E-setup. `file:///C:/Users/Hello/OneDrive/Desktop/Delta%20E-E/10_DeltaE_preparationmaterial.pdf`

[2] Bethe-Bloch formula: Wikipedia `https://en.wikipedia.org/wiki/Bethe_formula`

[3] Landau distribution: Wikipedia `https://en.wikipedia.org/wiki/Landau_distribution`

[4] Semiconductor detectors: `https://www.hep.physik.uni-siegen.de/teaching/masterlab/manuals/semiconductor_lab_FEI4.pdf`

[5] Linear interpolation:
`https://www.toppr.com/guides/maths-formulas/linear-interpolation-formula/#:~:text=Linear%20interpolation%20is%20a%20method,of%20the%20given%20channel's%20estimates.`

[6] Standard atomic weight: `https://en.wikipedia.org/wiki/Standard_atomic_weight`

7   Appendix

Constants:

[1] $2\pi N_a r_e^2 m_e c^2 = 0.1535 \, \text{MeV} \, \text{cm}^2/\text{g}$

[2] Avogadro number $N_a = 6.022 \times 10^{23} mol^{-1}$

[3] Classical electron radius $r_e = 2.817 \times 10^{-13} \, \text{cm}$

[4] Electron mass $m_e = 511 \, \text{keV}/c^2$

[5] Mean excitation potential I $= 173$ eV for silicium as absorber

[6] Proton: A $= 1.007$ u, Z $= 1$, $m_P = 938.27$ MeV

[7] Deuterium: A $= 2.014$ u, Z $= 2$, $m_D = 1875.6563184$ MeV

[8] Tritium: A $= 3.016$ u, Z $= 3$, $m_T = 2809.385904$ MeV

[9] Helium-3: A $= 3.016$ u, Z $= 3$, $m_{He} = 2809.385904$ MeV

[10] Alpha particle: A $= 4.002$ u, Z $= 2$, $m_\alpha = 3728.3978844000003$ MeV

[11] Lithium: A $= 7.016$ u, Z $= 7$, $m_{Li} = 6465.499854$ MeV

Linear interpolation

$$y = y_1 + \frac{(x - x_1)(y_2 - y_1)}{x_2 - x_1}$$